ACS APPLIED MATERIALS & INTERFACES

Research Article

www.acsami.org

Facile Route to an Efficient NiO Supercapacitor with a Three-Dimensional Nanonetwork Morphology

Sun-I Kim, Jung-Soo Lee, Hyo-Jin Ahn, Hyun-Kon Song, and Ji-Hyun Jang*

Interdisciplinary School of Green Energy and Low Dimensional Carbon Materials Center, UNIST, Korea

Supporting Information

ABSTRACT: NiO nanostructures with three distinct morphologies were fabricated by a sol–gel method and their morphology-dependent supercapacitor properties were exploited. The nanoflower- shaped NiO with a distinctive three-dimensional (3D) network and the highest pore volume shows the best supercapacitor properties. The nanopores in flower-shaped nanostructures, offering advantages in contact with and transport of the electrolyte, allow for 3D nanochannels in NiO structure, providing longer electron pathways. The XPS and EIS data of the NiO nanostructure confirm that the flower-shaped NiO, which has the lowest surface area among the three morphologies, was effectively optimized as a superior electrode and yielded the greatest pseudocapacitance. This study indicates that forming a 3D nanonetwork is a straightforward means of improving the electrochemical properties of a supercapacitor.

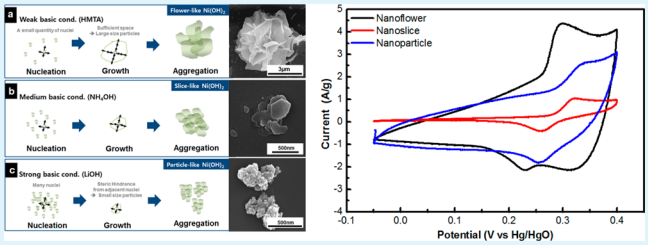

KEYWORDS: *NiO, $Ni(OH)_2$, morphology-dependent properties, nanostructure, three-dimensional networks, mesopores*

INTRODUCTION

With the rapid development of electronic devices, new energy storage systems with high capacitance and quicker charge/discharge rates in a small volume are required. Among many promising methods, some of the most practical systems for energy storage are fuel cells, secondary batteries, and capacitors. In particular, supercapacitors have attracted much attention because of their long life cycle and high power density.[1−6] Compared to electrical double layer capacitors (EDLC) operating in a double layer formed on the electrode surface, which limits the specific capacitance and leads to lower energy density relative to their theoretical value,[7,8] pseudocapacitors[9−12] using the oxidation−reduction reaction provide 3−4 times higher capacitance, because they not only react at the surface but also near the surface of the active electrode. In general, pseudocapacitors use conducting carbon polymers, which offer the advantages of an environmentally benign nature, low cost, a high voltage window, and high storage capacity.[13,14] Nevertheless, they are not suitable for practical application because of their poor stability; with progressive cycling, swelling and shrinkage of the conducting polymer occurs during charging/discharging cycles, which causes degradation of the electrode and fade-out of the electrochemical performance.[15] Compared to carbon materials, metal oxides have higher energy density and better stability.[16] Among metal oxides, RuO_2 has been widely researched because of its superior electrochemical properties such as high proton conductivity and a highly reversible redox process.[17,18] However, its practical applicability is impeded by the high costs of the initial materials. Alternatively, cost-effective nickel oxide (NiO) has been suggested as a promising electrode material because of its outstanding theoretical specific capacitance of 3750 F/g^{-17} and thermal stability.

Generally, the specific capacitance of a metal oxide increases notably with an increase in its surface area, because a large surface area is associated with more Faradic active sites and in turn higher pseudocapacitance. To date, the morphology of NiO and its controlled synthesis has been greatly important for its electrochemical performance as morphology is closely related to the specific surface area. From this point of view, a variety of porous nanostructures with large surface areas have been synthesized via surfactant-template, sol–gel, anodization, and hard template methods. For instance, the Rao group has reported the improved morphology and supercapacitance performance of microwave synthesized NiO, and the Yan group has exploited the surface area-dependent capacitance properties of NiO nanostructures with three different morphologies.[19,20] However, there have been few systematic studies on the unique morphology-dependent supercapacitance properties against characteristics of surface area.

In this article, we report a facile and controlled method to prepare various types of porous NiO nanostructures with fairly different morphologies such as flower-, slice-, and particle shapes, which show morphology-dependent capacitance properties. We demonstrate that the electrochemical properties vary depending on the connectivity of the crystallites and the portion of effective active sites of each sample rather than on the surface area itself. We further demonstrate that flower-shaped NiO having the lowest surface area to weight ratio can

Received: October 2, 2012
Accepted: February 1, 2013
Published: February 1, 2013

Scheme 1. Schematic Diagram Showing the Formation Process of (a) Flower-, (b) Slice-, and (c) Particle-like $Ni(OH)_2$ under Dfferent pH Conditions; Corresponding SEM Images of As-Prepared Samples are in the Right Panel

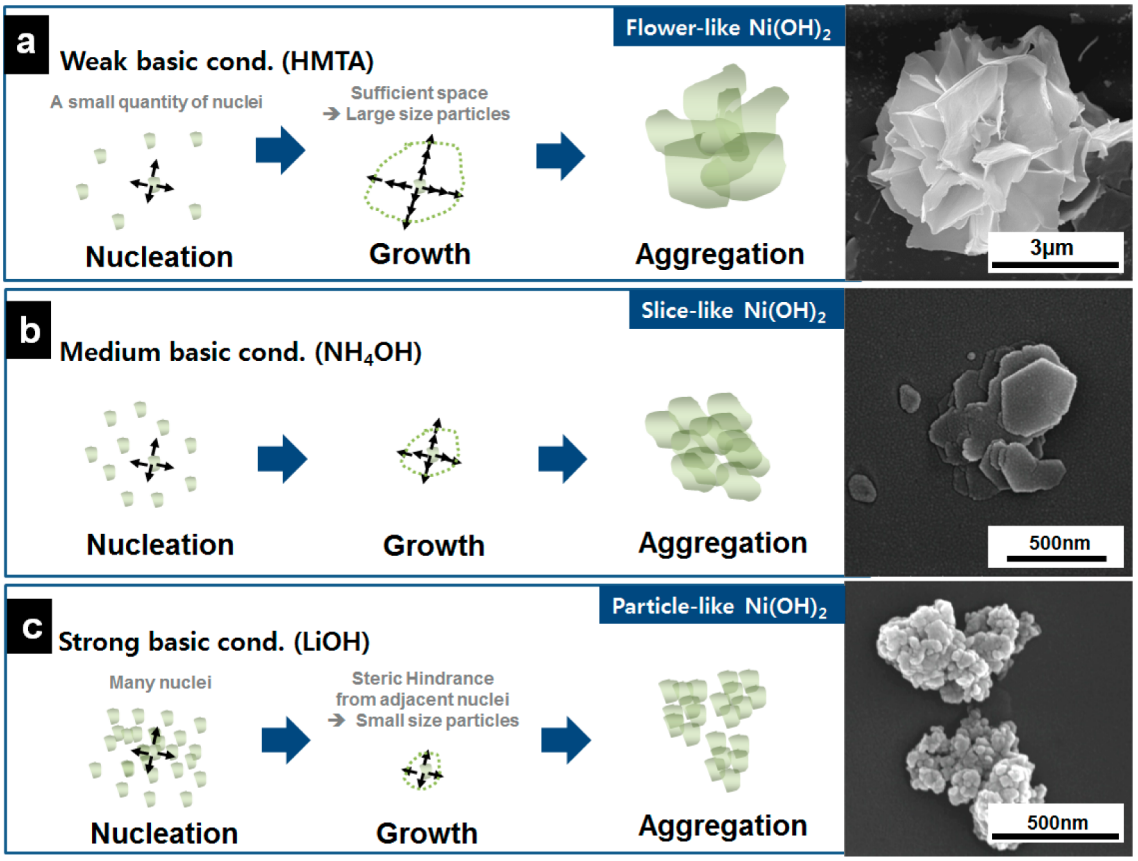

become a superior electrode with the greatest pseudocapacitance.

RESULTS AND DISCUSSION

A schematic diagram illustrating the creation of $Ni(OH)_2$ with specific morphologies prepared under different conditions is provided in Scheme 1, along with the corresponding SEM images. The SEM images reveal that $Ni(OH)_2$ nanostructures with three distinct shapes (nanoflower, nanoslice, and nanoparticle) can be synthesized simply by changing the base and the Ni precursor. For example, a flower-shaped $Ni(OH)_2$ nanostructure with diameters of about 3−5 μm was created in HMTA solution (Scheme 1a), whereas nanoslice-shaped $Ni(OH)_2$ with a diameter ranging from 300−530 nm (Scheme 1b) was synthesized in NH_4OH solution. By changing the acidity to strongly basic using LiOH, the size of the $Ni(OH)_2$ nanostructure was decreased to smaller nanoparticles with a diameter of around 50 nm (Scheme 1c). The different morphologies of $Ni(OH)_2$ can be attributed to the dissociation rate of the base, which determines the kinetics of the reaction between dissociated OH and the counterions of the nickel precursor. The formation process for $Ni(OH)_2$ starts from the exchange reaction of counterions of Ni^{2+} with dissociated OH^- creating small nuclei, followed by aggregation/self-assembly into larger particles with a particular crystal orientation and morphology, which is driven by the force to minimize the surface energy.[21] A nanoslice as shown in Scheme 1b is a commonly created shape formed by simple stacking of hexagonal shaped nanoplates in a medium alkaline solution. On the other hand, a weaker basic HMTA generates OH^- very slowly and forms a relatively small number of nuclei, providing the nuclei with sufficient time and space to increase the particle size (Scheme 1a).[22] This leads to the creation of larger size flower-shaped $Ni(OH)_2$ with an energetically favored state, which can be explained by Ostwald ripening.[21,23] In the case of the strongest base, i.e., LiOH, with a fast dissociation rate of OH^-, a large amount of OH^- in the reaction medium initiates the formation of a large number of $Ni(OH)_2$ nuclei at the initial stage. As a result, further growth of the nuclei into larger particles cannot take place due to the limited amount of precursors in the solution as well as steric (or spherical) hindrance from the adjacent nuclei, thus resulting in relatively small size particles (Scheme 1c). On the basis of this assumption, we could reproducibly control the shape of $Ni(OH)_2$ simply by changing the basicity of the solution.

$Ni(OH)_2$ has been reported to be a suitable solid-state precursor for porous NiO with high capacitance. During the calcination process of the $Ni(OH)_2$ precursors at 300 °C for 2 h, decomposition occurred accompanied by the conversion of $Ni(OH)_2$ into NiO nanocrystals. To investigate the thermal behavior during calcination, we examined TGA and DTA in an air condition in a temperature range from 100 to 800 °C with a heating rate of 10 °C/min. There is one major drop of the mass in each sample, but with slightly different onset points: 243, 284, and 280 °C for the nanoflower, nanoslice, and nanoparticl eshapes, respectively. The weight loss is due to the elimination of the hydroxy group by evaporation of water molecules, resulting in pore generation.[19] The onset temperature for degradation varies according to the binding energy between the Ni center atom and hydroxyl counterion. Based on the onset

dx.doi.org/10.1021/am3021894 | ACS Appl. Mater. Interfaces 2013, 5, 1596−1603

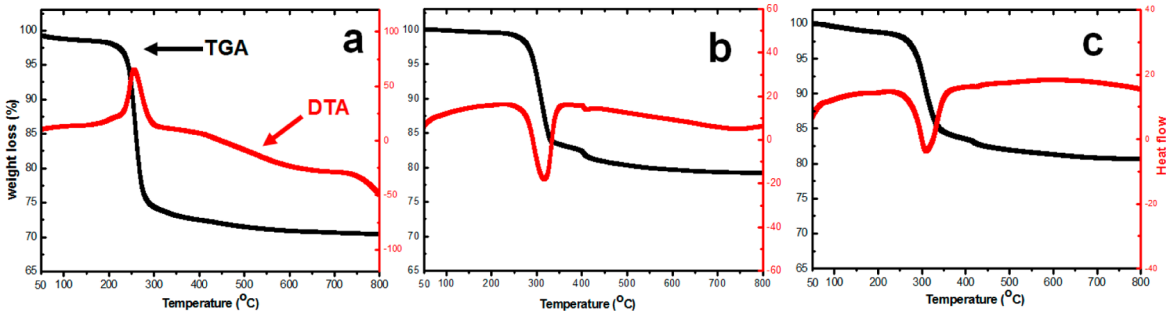

Figure 1. TGA and DTA curves of as-prepared $Ni(OH)_2$ nanostructures: (a) nanoflower, (b) nanoslice, and (c) nanoparticles.

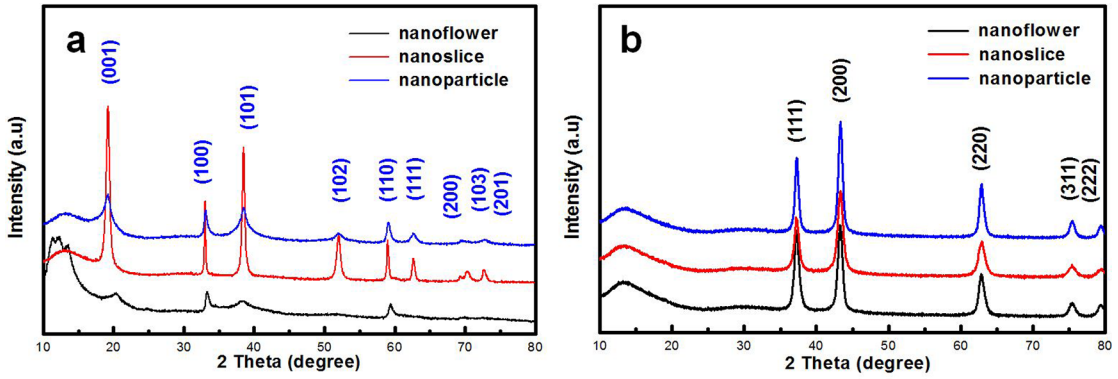

Figure 2. XRD pattern of the obtained (a) $Ni(OH)_2$, and (B) NiO nano structures with nanoflower, nanoslice, and nanoparticle shapes.

points, we hypothesize that the bond strength between Ni and OH in the nanoflower is the weakest whereas that in the nanoslice is the strongest. This can be explained by the fact that the crystallinity of the nanoflower is in the alpha phase where additional loosely bound intercalated water molecules in the interlayer gap are present; this will be discussed in the next section in connection with XRD data. The peak position in the DTA plot matches the temperature of the first derivative of the TGA curve, where structural change occurs. Interestingly, heat is emitted during the transformation from nanoflower-shaped $Ni(OH)_2$ into NiO, whereas the transformation for $Ni(OH)_2$ with the nanoslice and nanoparticle shapes requires heat absorption,[24] likely due to the greater binding energy between OH and the Ni center atom. Importantly, the degree of weight loss until the weight stabilizes in the nanoflower is 10% greater than that of the nanoslice and nanoparticle configurations (30% vs ~20%). The lower onset point and the greater loss in mass in the nanoflower structure can be ascribed to the enthalphic gain due to weak bonding between Ni and OH as well as entropic gain obtained by liberating the water molecules. On the contrary, the entropic gain was negatively compensated by the great loss in enthalphic energy leading to a lesser amount of weight loss as well as a high onset point in both nanoslice and nanoparticle-shaped $Ni(OH)_2$ with tight bonding between Ni and OH.

Figure 2 shows the XRD patterns of $Ni(OH)_2$ before and after sintering at 300 °C for 2 h in an air condition, confirming the transformation of $Ni(OH)_2$ into NiO nanostructure. The XRD peaks in black can be identified as those of a pure hexagonal phase of α-$Ni(OH)_2$, on the basis of the standard pattern in JCPDS card 22−0444, whereas all detectable peaks in the red and blue curves of Figure 2a can be indexed to a single phase of β-$Ni(OH)_2$ (JCPDS card 14−117). These results are interesting in that the phase of crystallites of $Ni(OH)_2$ is directly related with opposite behaviors in the sign of enthalphic energy during the transformation, as shown in previously discussed DTA data (Figure 1). For instance, the alpha phase of $Ni(OH)_2$ implies the negative enthalpy ($\Delta H < 0$), which can be explained by the ability to facilitate the evaporation of water to form NiO. Compared to the beta phase with an ordered stacking layer of $Ni(OH)_2$, the alpha form is a hydroxyl-deficient phase stacked with $Ni(OH)_{2-x}$ layers and with intercalated water molecules in the interlayer space. This is consistent with the relatively lower intensity of XRD peaks, implying low crystallinity and small single-crystal size of $Ni(OH)_2$ in the alpha phase. Consequently, the DTA data could provide an auxiliary way to judge the phase of $Ni(OH)_2$ without measuring XRD. The XRD pattern at the peak positions of 2θ = 37, 43.4, 62.8, 75.5, and 79.8° in Figure 2b corresponds to the (111), (200), (220), (311), and (222) planes of the NiO (JCPDS card 04−0835) and the sharp peaks confirm the large size of crystals of NiO regardless of the phase of the corresponding $Ni(OH)_2$ precursor. Additionally, the XRD pattern verifies the purity of as-prepared $Ni(OH)_2$ and NiO nanostructures, as shown in panels a and b in Figure 2.[25]

Pore generation due to the thermal decomposition of $Ni(OH)_2$ can be confirmed by SEM, HR-TEM images, and BET data, as shown in Figure 3. The SEM images reveal that the external morphologies as well as dimensions of $Ni(OH)_2$ are nearly maintained except for the occurrence of additional pore opening. Close inspection via HR-TEM confirms the pore size of NiO nanostructures with mean diameters of 16, 6, and 8 nm, corresponding to nanoflowers, nanoslices, and nanoparticles, respectively. The crystallinity is verified by clear lattice fringes with the spacing of about 0.21 and 0.24 nm, which corresponds to the (200) and (111) planes of cubic crystalline NiO. It should be noted that the nanoflower-shaped NiO has a distinct morphology in a three-dimensionally interconnected

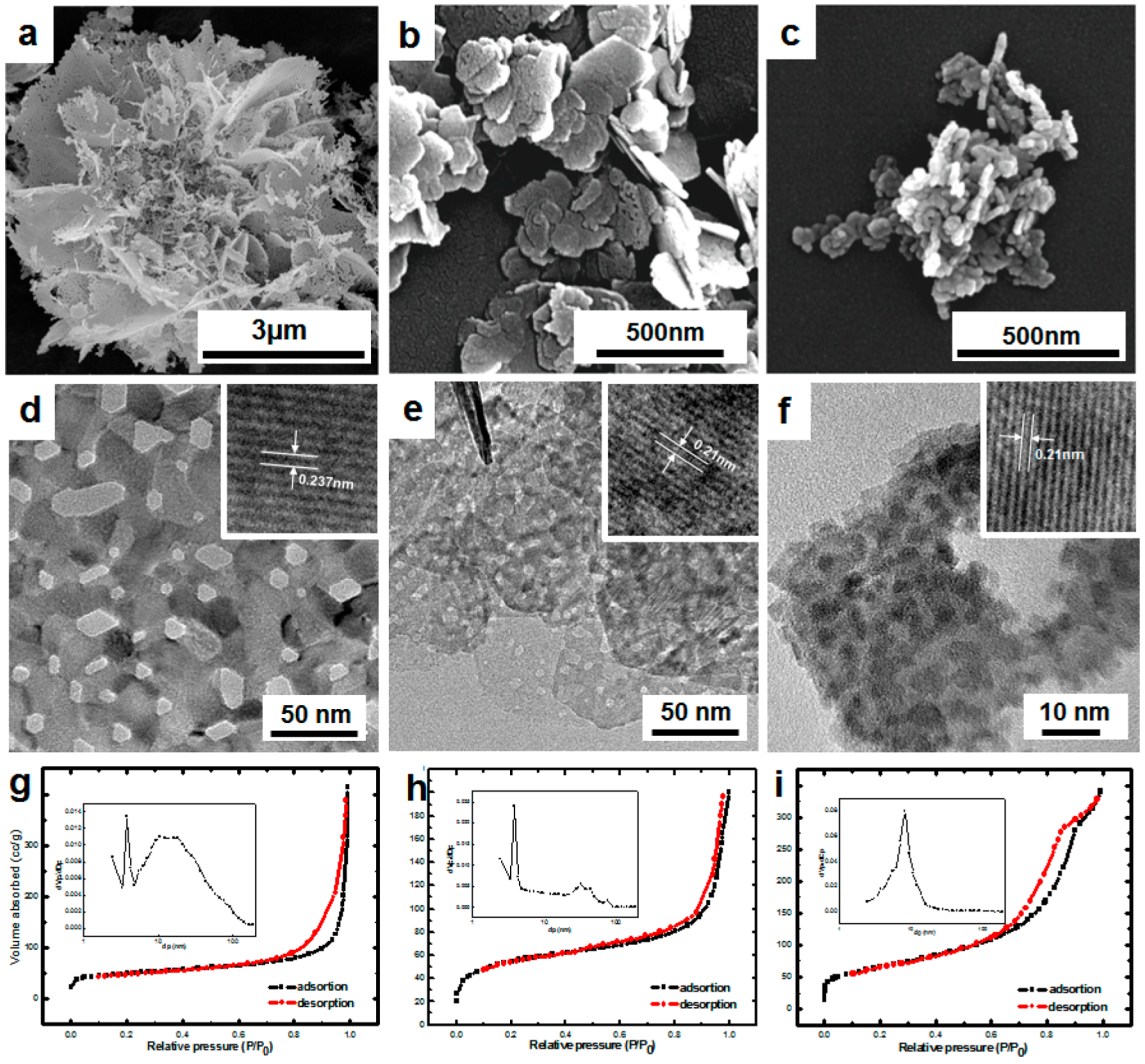

Figure 3. (a–c) SEM image, (d–f) HRTEM image, and (g–i) nitrogen adsorption–desorption isotherm of NiO nanostructures created from thermal decomposition of $Ni(OH)_2$: (a, d, g) NiO nanoflower, (b, e, h) nanoslice, and (c, f, i) nanoparticle. The insets in g, h, i are the BHJ pore size distribution plots.

structure, whereas the nanoslice or nanoparticle-shaped NiO has a nanoporous morphology with disconnection between each thin layer.

Nitrogen adsorption/desorption isotherms of the NiO nanostructures are shown below the corresponding TEM images. The isotherm of NiO with nanoflower, nanoslice, and nanoparticle shapes is type IV and shows a narrow hysteresis loop at a low relative pressure, indicating that the mesoporous structure is fairly open and there is no significant impediment to the capillary evaporation with respect to the capillary condensation of nitrogen.[26] Table 1 demonstrates that the BET specific surface area of nanoflower, nanoslice, and nanoparticle NiO is 159, 193, and 233 m^2/g and the average pore size is 16.7, 6.3, and 8.8 nm, respectively, which is in accordance with the TEM image. The mesopores are attributed to the void space among the stacked NiO nanocrystals generated by the thermal evaporation of water molecules. Because of having the largest dimensions of structure and pore size, the nanoflower-shaped NiO has the lowest surface area, but the largest pore volume, whereas nanoparticles show the greatest surface area due to that nanostructure having the smallest dimension. Compared to the nanoflower and nanoparticle NiO structures, the nanoslice structure may not be favored as an active material because it could further reduce the effective specific surface area induced by compact stacking of each layer, leading to capacitance fading.[27] The pore size distributions of NiO vary according to the morphology of the structure and packing. Compared to nanoslices and nanoparticles mostly having small size mesopores with apparent pore diameters of 3.8 and 8 nm, respectively, the nanoflower-shaped NiO presents a bimodal-type pore size distribution with maxima peaks centered at ~3.8 and ~15 nm, while maintaining the adequate surface area. The samples have not only many small size pores (below 5 nm), but also a significant amount of larger size mesopores (above 10 nm), which allows improved permeability of electrolytes (see Scheme S1 in the Supporting Information). Furthermore, the

Table 1. Surface Area, Total Pore Volume, and BJH Pore Size of NiO Nanostructure

	nanoflower	nanoslice	nanoparticle
surface are (m^2/g)	159	193	233
pore size (nm)	16.7	6.3	8.8
total pore volume (cm^3/g)	0.66	0.30	0.51

dx.doi.org/10.1021/am3021894 | ACS Appl. Mater. Interfaces 2013, 5, 1596–1603

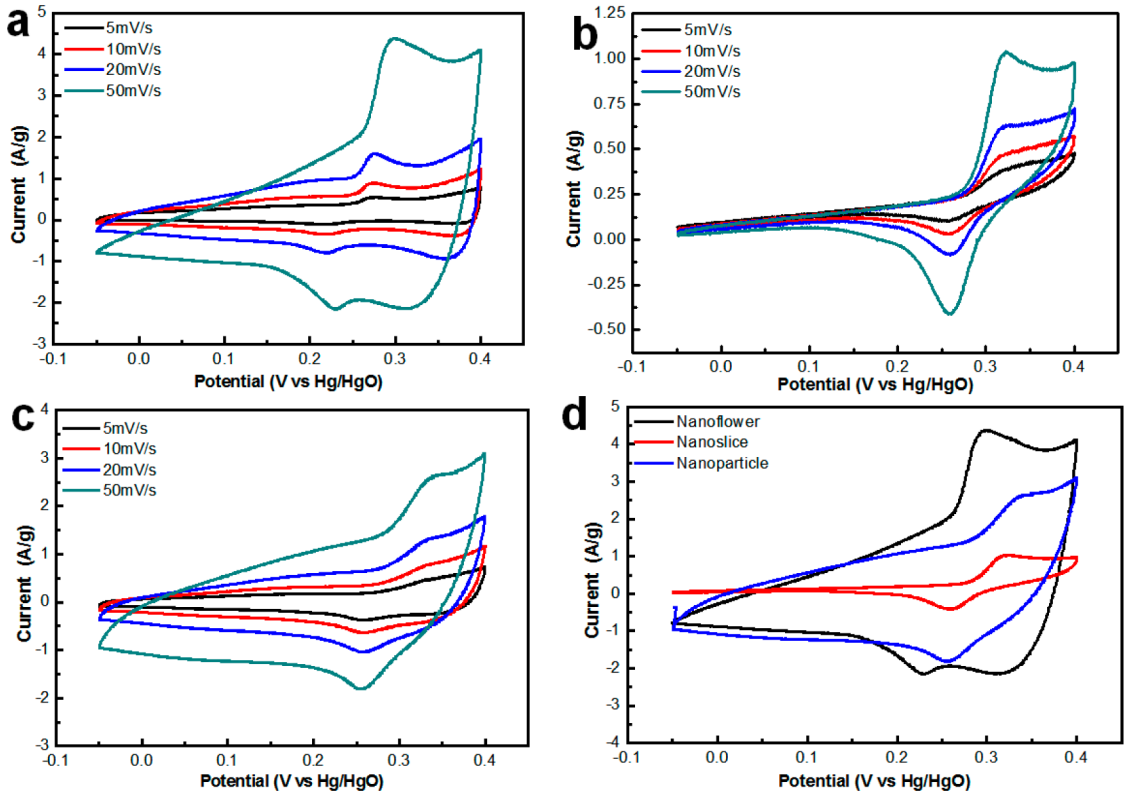

Figure 4. Cyclic voltammogram curve of the capacitor at different scan rates of NiO nanostructure: (a) nanoflower, (b) nanoslice, and (c) nanoparticle. (d) Comparison of CV curves of three different shaped NiO nanostructures at a scan rate of 50 mV/s.

large quantity of adsorbed N_2 gas at p/p_0= 0.9−1.0 implies the presence of a relatively large fraction of macropores,[19] which can be attributed to the interparticle distances in nanoflower-shaped NiO. This relatively loosely packed morphology nonetheless features firm connections between nanoparticles, as shown in the SEM image (see Figures S4 and S5 in the Supporting Information), which leads to improved electrolyte permeability and facilitates the formation of three-dimensional networks with enhanced electron pathways, thus potentially improving the pseudocapacitance.

On the basis of these morphological studies, cyclic voltammogram tests on the NiO nanostructures as active materials for a supercapacitor were performed at different scan rates to observe the CV curve change depending on the shape of the nanostructure, as shown in Figure 4. The CV curves show typical cathodic and anodic peaks arising during the redox reaction (in eq 1) between NiO and NiOOH, as commonly observed for a pseudocapacitor.[28]

$$\mathrm{NiO} + \mathrm{OH}^- \underset{\text{discharge}}{\overset{\text{charge}}{\rightleftharpoons}} \mathrm{NiOOH} + \mathrm{e}^- \quad (1)$$

The unsymmetrical redox peaks of respective NiO configurations indicate the irreversibility of the redox processes, which is common for a pseudocapacitor, where ions are charged and discharged continuously and the electrolyte diffuses in the porous electrode, inducing ohmic resistance and polarization during the redox reaction. The ΔE_p ($E_{pa} - E_{pc}$) is a readily measurable value for evaluating the reversibility of the redox reaction. The nanoflower shape NiO shows the greatest reversibility, with the lowest ΔE_p of 54 mV, whereas that of the nanoslice and nanoparticle specimens is 61 and 71 mV, respectively, as described in Table 2. With increasing scan rate, the area of the CV curve is increased. The NiO nanoflower structure with the greatest reversibility (lowest ΔE_p) shows the largest area of the CV curve at a scan rate of 50 mV, indicating that the nanoflower structure has higher capacitance than the other nanostructures, as shown in Figure 4d.

Table 2. Potentials for Different NiO Morphologies: Anodic Peak Potential (E_{pa}), Cathodic Peak Potential (E_{pc}), and ΔE_p at a Scan Rate of 50 mV/s

sample	E_{pa} (mV)	E_{pc} (mV)	ΔE_p (mV)
nanoflower	324	270	54
nanoslice	372	311	61
nanoparticle	382	311	71

The accurate specific capacitance of different morphologies of NiO is calculated from the galvanostatic discharge curves based on eq 2,[29] as shown in Figure 5.

$$C = I\Delta t/m\Delta V \quad (2)$$

When comparing the discharge curves of different shapes of NiO, the NiO nanoflower shows longer discharge time than the nanoslice and nanoparticle morphologies, indicating that the nanoflower structure has better charge storage performance among NiO nanostructures. Unexpectedly great specific capacitance values of 480, 381, 333, and 252 F/g at current densities of 0.5, 1, 2, and 5 A/g, respectively were recorded for the NiO nanoflower. These values are much higher than those of other structures with greater surface areas; the nanoslice shows values of 116, 86, 65, and 52 F/g, and the nanoparticle gives values of 260, 235, 179, and 89 F/g at current densities of 0.5, 1, 2, and 5 A/g. Furthermore, the slope of the curve of the specific capacitance retention value with increasing current density is much lower for the nanoflower shape NiO sample

dx.doi.org/10.1021/am3021894 | ACS Appl. Mater. Interfaces 2013, 5, 1596−1603

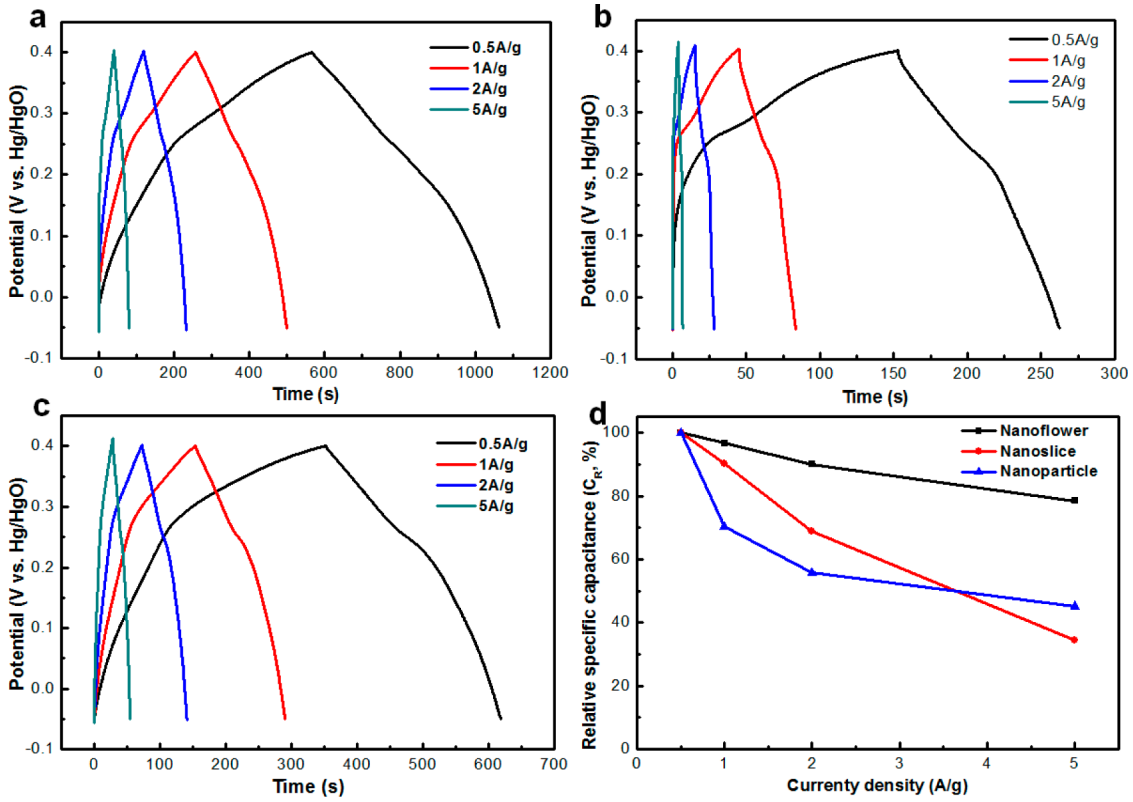

Figure 5. Discharging curve of the NiO supercapapcitor at different discharge current densities: (a) nanoflower, (b) nanoslice, and (c) nanoparticle-shaped nanostructures. (d) Comparison of capacitance retention of the NiO supercapacitors with three different morphologies.

than for the other two samples as shown in Figure 5d. This can be explained by the superior surface characteristics of the nanoflower-shaped NiO structure, despite having the lowest surface area. The nanoflower-shaped structure is advantageous in that it has distinct three-dimensional networks (as verified by the TEM image) that provide electrons longer diffusion paths, passing through the nanochannels in NiO nanostructures. Moreover, the nanoflower has the greatest portion of pore volume in which water molecules are absorbed. It has been reported that the nanopores in metal oxide can behave as a buffering reservoir to accommodate OH^- ions for the redox reaction, providing conducting pathways with the capability of facilitating maximized contact and fast diffusion and therefore enhanced kinetics of the reversible redox process for charge storage.[30−32] Compared to nanoslice and nanoparticle-shaped NiO with lower pore volumes, the nanoflower-shaped NiO nanostructure has large electroactive surface sites for better electrolytic contact, resulting in the highest charge storage capacity among the fabricated morphologies. On the basis of these results, we propose that the portion of pore volume with suitable pore size and the three-dimensional connectivity in the NiO nanostructure are more important factors than the surface area.

To quantify the amount of water molecules present in the NiO nanostructures, which helps the transportation of electrolyte ions, we analyzed X-ray photoelectron spectroscopy (XPS) spectra of oxygen in the samples. As shown in Figure 6a−c, the O 1s core level curves of thermally prepared NiO display two distinct maxima, located at 528−529, 530, and a slight tail at the 531−532 eV region. The peak at 528 eV is attributed to O^{2-} (oxygen bound to nickel), whereas the peaks at 530 and 531−532 eV are attributed to defective sites and to H_2O, chemically and physically bounded water molecules at the surface of NiO, respectively.[31,33−35] The comparison of the water contents (OH^- and H_2O) in the curve fitting spectra indicates that the nanoflower-shaped NiO is a more hydrous compound than the nanoslice and nanoparticle specimens, probably because of the greater portion of pore volume, providing an easy OH^- transport pathway in the nanoflower structure. The improved charge transfer and faster ion transport behavior of the nanoflower structure is further confirmed by the results of the electrochemical impedance spectroscopy (EIS) analysis. As shown in the Nyquist plot in Figure 6d, the nanoflower-shaped NiO exhibits a slightly larger semicircle than the nanoparticles at the high-frequency region and a lower slope in the medium-frequency region as compared to the nanoparticles and nanoslices. The diameter of the semicircle at the high-frequency region corresponding to the charge transfer resistance at the interface between the oxide and electrolyte implies that the nanoflower has a bit greater resistance. This appears to be attributable to long-range disconnectivity between flower-shaped particles of large dimension. However, the smaller second partial semicircle at the medium frequency region, corresponding to the charge transfer resistance for the Faradaic redox process, which is greatly affected by the surface morphology of NiO, implies that the nanoflower has the lowest resistance for the Faradic reaction, which is facilitated by the improved conductivity in the three-dimensionally interconnected nanostructure and the greater amount of intercalated water molecules in the greater portion of pore volume helping the diffusion of the OH.

dx.doi.org/10.1021/am3021894 | ACS Appl. Mater. Interfaces 2013, 5, 1596−1603

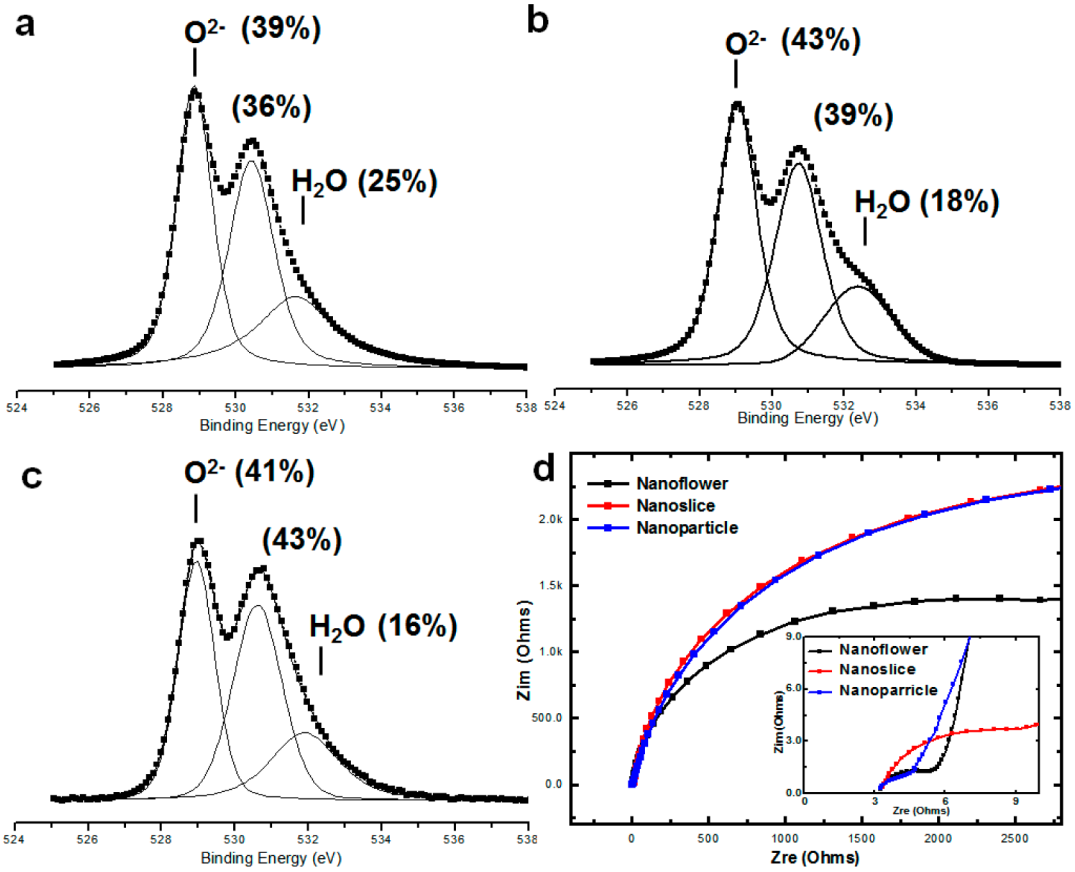

Figure 6. XPS spectra of O 1s regions of NiO nanostructures with (a) nanoflower, (b) nanoslice, and (c) nanoparticle shapes. The percentage numbers inside the graph indicate the percentage of integrated area determined by deconvolution. (d) Nyquist plots (Z_{re} vs Z_{im}) for three different NiO structures. The inset is a close-up image of the EIS plots in the high frequency region.

CONCLUSIONS

We have successfully synthesized porous NiO nanostructures with three distinct morphologies by thermal decomposition of a $Ni(OH)_2$ precursor. The morphology of as-prepared $Ni(OH)_2$ is simply directed by controlling the pH of the solution. Electrochemical measurements showed that the nanoflower-shaped NiO, having the greatest pore volume but the lowest surface area, exhibited the greatest specific pseudocapacitance. The excellent performance of the nanoflower-shaped NiO 3D nanonetwork can be attributed to the many pores, which allow easy contact with and transportation of the electrolyte and the formation of nanochannels in the NiO structure, in turn providing longer electron pathways. This hypothesis is well-supported by the XPS and EIS data of the NiO nanostructure. Our findings will offer extensive data for the design of high performance capacitance materials.

METHODS

Synthesis of Various $Ni(OH)_2$ Nanostructures. All chemicals in this work were purchased from Sigma Aldrich Co. were of analytical grade, and were used without any further purification. $Ni(CH_3COO)_2{\cdot}H_2O$ and $Ni(NO_3)_2{\cdot}6H_2O$ were used as $Ni(OH)_2$ precursors and ammonium hydroxide (NH_4OH), lithium hydroxide (LiOH), and hexamethylene tetramine (HMTA) were used to control the reaction conditions. In a typical synthesis of a $Ni(OH)_2$ flower nanostructure, 100 mmol of $Ni(NO_3)_2{\cdot}6H_2O$ and 100 mmol of HMTA were dissolved in deionized water under magnetic stirring. To prepare nanoslice and nanopaticle $Ni(OH)_2$, we used 100 mmol of $Ni(CH_3COO)_2{\cdot}H_2O$; 4 mL of NH_4OH and 100 mmol of LiOH were respectively added in the $Ni(CH_3COO)_2{\cdot}H_2O$ solution instead of HMTA to control the acidity of the solution. Each solution was then transferred into a 100 mL Teflon container, maintained at 100 °C for 4 h, and then cooled naturally. The synthesized nickel hydroxide products were cleaned by centrifuging and washing with distilled water and ethanol. The as-prepared samples were finally dried under a vacuum at 60 °C for 8h.

Synthesis of Various Porous NiO Nanostructures. Porous NiO nanostructure powders were obtained by annealing as-prepared $Ni(OH)_2$ samples at 300 °C for 2 h. After calcination, a color change from light green to gray was visualized, confirming the transformation of $Ni(OH)_2$ into NiO.

Characterization. The purity and crystallinity of the synthesized samples were characterized using X-ray diffraction (XRD, Bruker D8 advance) with Cu Ka radiation (λ = 1.5406 A) at a scan rate of 1°/s in the 2θ range from 10° to 80°. To measure the phase transformation temperature of the synthesized $Ni(OH)_2$, a thermogravimetric analysis (TGA) and a differential thermal analysis (DTA) were carried out on an SDT Q 600, employing a heating rate of 10 °C min^{-1}. The microscopic features of the $Ni(OH)_2$ and NiO powder nanostructures were characterized by scanning electron microscopy (SEM, FEI/USA Nanonova 230) and high-resolution transmission electron microscopy (FETEM, JEOL TEM 2100) at an accelerating voltage of 200 kV. The surface properties such as specific surface area, pore size, and pore volume were analyzed using the Brunauer–Emmett–Teller (BET) method with a Belsorp max (Bel Japan).

Electrochemical Tests. The working electrode was prepared by mixing the electro-active material (NiO, 85 wt %), acetylene black (10 wt %), and polyvinylidene difluoride (PVDF, 5 wt %) as a binder. The mixture was then pasted onto a Ni electrode and dried at 200 °C in an air atmosphere for 20 min. The electrochemical performance of the nanostructured NiO was evaluated using Pt foil as a counter electrode

and a KOH solution (2 M) as an electrolyte. Galvanostatic charge–discharge and cyclic voltammetry were measured using a computer controlled electrochemical interface (Solartron SI 1287) and a potentiostat (Versa STAT 3, AMETEK) from −0.05 V to 0.4 V at room temperature.

■ ASSOCIATED CONTENT

Ⓢ Supporting Information

The table of BET and XPS data, the capacitance performance data, the scheme of a plausible mechanism for ion diffusion, SEM images of the final electrodes, and FT-IR data of nanoflower shaped-nickel oxide and the precursors. This material is free of charge via Internet at http://pubs.acs.org.

■ AUTHOR INFORMATION

Corresponding Author

*E-mail: clau@unist.ac.kr .

Notes

The authors declare no competing financial interest.

■ ACKNOWLEDGMENTS

This work is supported by NRF with Contract NRF-2010-0019408, NRF-2012-0002413, and supported by NRF through the human resource training project for regional innovation.

■ REFERENCES

(1) Liu, C.; Li, F.; Ma, L. P.; Cheng, H. M. *Adv. Mater.* **2010**, *22*, E28–E62.
(2) Wei, T. Y.; Chen, C. H.; Chien, H. C.; Lu, S. Y.; Hu, C. C. *Adv. Mater.* **2010**, *22*, 347–351.
(3) Seo, E.; Lee, T.; Lee, K. T.; Song, H. K.; Kim, B. S. *J. Mater. Chem.* **2012**, *22*, 11598–11604.
(4) Candelaria, S. L.; Garcia, B. B.; Liu, D. W.; Cao, G. Z. *J. Mater. Chem.* **2012**, *22*, 9884–9889.
(5) Su, F. B.; Poh, C. K.; Chen, J. S.; Xu, G. W.; Wang, D.; Li, Q.; Lin, J. Y.; Lou, X. W. *Energy Environ. Sci.* **2011**, *4*, 717–724.
(6) Li, J. T.; Zhao, W.; Huang, F. Q.; Manivannan, A.; Wu, N. Q. *Nanoscale* **2011**, *3*, 5103–5109.
(7) Wang, G. P.; Zhang, L.; Zhang, J. *J. Chem. Soc. Rev.* **2012**, *41*, 797–828.
(8) An, K. H.; Kim, W. S.; Park, Y. S.; Moon, J. M.; Bae, D. J.; Lim, S. C.; Lee, Y. S.; Lee, Y. H. *Adv. Funct. Mater.* **2001**, *11*, 387–392.
(9) Wang, Y. G.; Li, H. Q.; Xia, Y. Y. *Adv. Mater.* **2006**, *18*, 2619–2623.
(10) Tian, X. Q.; Cheng, C. M.; Qian, L.; Zheng, B. Z.; Yuan, H. Y.; Xie, S. P.; Xiao, D.; Choi, M. M. F. *J. Mater. Chem.* **2012**, *22*, 8029–8035.
(11) Xia, X. H.; Tu, J. P.; Wang, X. L.; Gu, C. D.; Zhao, X. B. *J. Mater. Chem.* **2011**, *21*, 671–679.
(12) Jiang, H.; Li, C. Z.; Sun, T.; Ma, J. *Nanoscale* **2012**, *4*, 807–812.
(13) Fan, L. Z.; Maier. *J. Electrochem. Commun.* **2006**, *8*, 937–940.
(14) Prasad, K. R.; Koga, K.; Miura, N. *Chem. Mater.* **2004**, *16*, 1845–1847.
(15) Li, L.; Loveday, D. C.; Mudigonda, D. S. K.; Ferraris, J. P. *J. Electrochem. Soc.* **2002**, *149*, A1201–A1207.
(16) Xia, X. H.; Tu, J. P.; Zhang, Y. Q.; Wang, X. L.; Gu, C. D.; Zhao, X. B.; Fan, H. J. *ACS Nano*, *6*, 5531-5538.
(17) Kim, I. H.; Kim, K. B. *J. Electrochem. Soc.* **2006**, *153*, A383–A389.
(18) Vellacheri, R.; Pillai, V. K.; Kurungot, S. *Nanoscale* **2012**, *4*, 890–896.
(19) Meher, S. K.; Justin, P.; Rao, G. R. *ACS Appl. Mater. Interfaces* **2011**, *3*, 2063–2073.
(20) Zhang, X. J.; Shi, W. H.; Zhu, J. X.; Zhao, W. Y.; Ma, J.; Mhaisalkar, S.; Maria, T. L.; Yang, Y. H.; Zhang, H.; Hng, H. H.; Yan, Q. Y. *Nano Res.* **2010**, *3*, 643–652.
(21) Cao, C. Y.; Guo, W.; Cui, Z. M.; Song, W. G.; Cai, W. *J. Mater. Chem.* **2011**, *21*, 3204–3209.
(22) Ren, Y.; Gao, L. A. *J. Am. Ceram. Soc.* **2010**, *93*, 3560–3564.
(23) Lou, X. W.; Yuan, C. L.; Rhoades, E.; Zhang, Q.; Archer, L. A. *Adv. Funct. Mater.* **2006**, *16*, 1679–1684.
(24) Zhu, L. P.; Liao, G. H.; Yang, Y.; Xiao, H. M.; Wang, J. F.; Fu, S. Y. *Nanoscale Res. Lett.* **2009**, *4*, 550–557.
(25) Lang, J. W.; Kong, L. B.; Wu, W. J.; Liu, M.; Luo, Y. C.; Kang, L. *J. Solid State Chem.* **2009**, *13*, 333–340.
(26) Condon, J. B. *Surface Area and Porosity Determinations by Physisorption: Measurements and Theory*, 1st ed.; Elsevier: Amsterdam, 2006.
(27) Ji, X. B.; Hallam, P. M.; Houssein, S. M.; Kadara, R.; Lang, L. M.; Banks, C. E. *RSC Adv.* **2012**, *2*, 1508–1515.
(28) Meher, S. K.; Justin, P.; Rao, G. R. *Nanoscale* **2011**, *3*, 683–692.
(29) Kaempgen, M.; Chan, C. K.; Ma, J.; Cui, Y.; Gruner, G. *Nano Lett.* **2009**, *9*, 1872–1876.
(30) Yuan, C. Z.; Zhang, X. G.; Su, L. H.; Gao, B.; Shen, L. F. *J. Mater. Chem.* **2009**, *19*, 5772–5777.
(31) Foelske, A.; Barbieri, O.; Hahn, M.; Kotz, R. *Electrochem. Solid-State Lett.* **2006**, *9*, A268–A272.
(32) Wen, J. G.; Ruan, X. Y.; Zhou, Z. T. *J. Phys. Chem. Solids* **2009**, *70*, 816–820.
(33) Dupin, J. C.; Gonbeau, D.; Vinatier, P.; Levasseur, A. *Phys. Chem. Chem. Phys.* **2000**, *2*, 1319–1324.
(34) Chigane, M.; Ishikawa, M. *J. Chem. Soc., Faraday Trans.* **1998**, *94*, 3665–3670.
(35) Norton, P. R.; Tapping, R. L.; Goodale, J. W. *Surf. Sci.* **1977**, *65*, 13–36.